

OCM2 vicarious calibration over cal-val sites: Little Rann of Kuchchh and Kavaratti



K. N. Babu, R. P. Prajapati, Moosa Ali, Anurag Gupta, A. K. Mathur
and Mini Raman

Calibration and Validation Division

EPSA/SAC

Ahmedabad – 380 015

June, 2018

Document control sheet

1. Report No.	SAC/EPISA/CVD/CAL-VAL/02/18
2. Publication date	June, 2018
3. Title and subtitle	OCM2 vicarious calibration over cal-val sites: Little Rann of Kuchchh and Kavaratti
4. Type of report	Scientific
5. Number of pages	29
6. Number of references	20
7. Authors	K. N. Babu, R. P. Prajapati, Moosa Ali, Anurag Gupta, A. K. Mathur and Mini Raman
8. Originating unit	CVD-EPISA
9. Abstract	Special campaigns were planned to carry out the vicarious calibration of OCM2 using ocean site (Kavaratti, Cal-Val site) on 27 th Feb. 2018, 1 st March 2018 and land site on 4 th January, 25 th March and 27 th March 2018 (Amarapur, Cal-Val site) respectively. OCM2 is over estimating the TOA radiances over both the sites. The land site TOA radiances are simulated with 6S vector radiative transfer model, which includes the polarization effect arising from Rayleigh and Mie particles. The ocean site TOA radiance are simulated through the radiative transfer calculation as described in this report, in this calculation the radiation due to polarization effect is not considered. Except for the first band, the gain coefficients vary from 0.85 to 0.94 in case of land target calibration exercise. The ocean target calibration coefficients vary from 0.76 to 0.84, while the band 8 gain coefficient is much lower.
10. Key words	Kavaratti, CAL-VAL site, optical parameters, Met. Observations
11. Security classification	Unrestricted
12. Distribution statement	General

Table of Contents

Document control sheet	2
1. Abstract	4
2. Introduction	4
3. Measurement plan	5
4. Satellite data used	15
5. Screening of data set for vicarious calibration	17
6. Methodology: vicarious calibration	18
6.1 High reflectance land target	18
6.2 Vicarious calibration (low reflectance ocean target)	22
7. Conclusion	27
8. Acknowledgements	27
9. References	27

1. Abstract

Special campaigns were planned to carry out the vicarious calibration of OCM2 using ocean site (Kavaratti, Cal-Val site) on 27th Feb. 2018, 1st March 2018 and land site on 4th January, 25th March and 27th March 2018 (Amarapur, Cal-Val site) respectively. OCM2 is over estimating the TOA radiances over both the sites. The land site TOA radiances are simulated with 6S vector radiative transfer model, which includes the polarization effect arising from Rayleigh and Mie particles. The ocean site TOA radiance are simulated through the radiative transfer calculation as described in this report, in this calculation the radiation due to polarization effect is not considered. Except for the first band, the gain coefficients vary from 0.85 to 0.94 in case of land target calibration exercise. The ocean target calibration coefficients vary from 0.76 to 0.84, while the band 8 gain coefficient is much lower.

2. Introduction

In order to correctly calibrate a spaceborne/airborne instrument and ensure data quality, we must understand how the at-aperture radiance spectra measured by the sensor are related to the reflectance spectra of the imaged surface and the effects of atmospheric propagation, solar illumination and sensor geometry on this relationship. Characterizing and understanding this relationship using invariant test sites is key to successful calibration when ground truth data are not available. Subsequent to satellite launch, a number of factors such as deep space environment, launch stresses, sensor ageing etc. can affect the performance of the sensor onboard a satellite. Sensor optics/detector degradation due to various causes can potentially lead to change in the calibration coefficients over time and hence, there is a need to monitor and document these changes periodically. Some satellites such as Landsat MSS and TM use on-board lamps or solar diffusers as internal calibrators, to monitor temporal drifts in calibration coefficients. However, these are also subject to degradation over time (Thome, 2001) and therefore, it is important to have an independent method to monitor sensor calibration coefficients. Vicarious calibration provides a method to derive sensor calibration coefficients from an estimate of top-of-the-atmosphere (TOA) at-satellite radiances which is completely independent from laboratory and on-board calibration mechanisms.

Vicarious calibration is important for airborne and spaceborne sensors because it is independent of the sensor and any onboard calibration system, but it requires personnel be present at a test site during the aircraft or satellite overpass. The ground-based data collection can be limited by poor weather, and also by the large travel distances from working office to the test sites. There are many methods of vicarious calibration, viz., absolute vicarious calibration, relative calibration, lunar calibration etc. that can be used to monitor possible variations in sensor calibration coefficients. Vicarious calibration refers to the process of determining a sensor calibration coefficient using field measured surface radiance/reflectance and sensor observed digital number (DN)/radiance values of the same surface, at the time of satellite pass. If the instruments used for making field measurements are traceable to NIST or other well-known standards, then the vicarious calibration becomes an absolute calibration. The field measured hyper-spectral surface reflectance at different wavelengths is averaged over the corresponding wavelength bands of the sensor and passed through an atmospheric transfer code to compute the TOA radiance or reflectance. The average radiance per DN (typically averaged over 3*3 or 5*5 pixels covering the study sites) in an image is computed and compared with estimated radiance per DN for the same pixels to derive vicarious calibration coefficients for different bands. This method has been applied to estimate vicarious post-launch calibration coefficients for Landsat ETM (Thome, 2001), Landsat and EO – 1, ALI sensors (Chander et al., 2009), AWiFS sensor (Pagnutti and Holekamp, 2006), MISR (Bruegge et al., 2007). This is only a representative list and not an exhaustive one. An equivalent method of computing vicarious calibration coefficients is to compute the ratio L_{est}/L_{obs} , where L_{est} and L_{obs} are the TOA estimated and sensor measured radiances respectively.

3. Measurement plan

The OCM2 sensor post launch quantitative radiometric performance is being monitored at Kavaratti site since its launch, year 2009. In this report radiometric two-point calibration using low reflectance target of Kavaratti site and high reflectance target of Rann of Kuchchh has been attempted through field campaign. To meet the objectives, the campaigns are designed on the following sites:

Site name	Nature of site	Field campaign dates
Kavaratti	Low reflectance	27 th February and 1 st March 2018
Amarapur	High reflectance	4 th January 2018, 27 th March 2018
Desalpar	High reflectance	25 th March 2018

The opportunities of AVIRIS-NG aerial hyper-spectral mission campaign helped us to plan and perform the multiple dates required for the OCM2 over the high reflectance target. The design of field campaign for two sensors gave a unique experience and also gave us additional constrain to expose for the sun heat. The details of site and method of vicarious calibration using high reflectance target is given by Sridhar et al., 2013. The list of instruments used during the filed campaign is listed in Table 1.

The field reflectance measurements were carried out at 25 locations (located in square grid of 5x5 pixels) within the site during the study period using the ASD FieldSpec4 Spectroradiometer (Analytical Spectral Devices). The hyperspectral target reflectance in 350 – 2500nm intervals was measured during the field campaigns. Though the spectral resolution of the instrument is 3nm, the output data is available spectrally at 1nm interval through post processing software (view-spec pro). In order to obtain a representative set of measurements for each site the reflectance measurements were attempted systematically at intervals of 350m for OCM2 sensor, while ensuring that they were completed within ± 30 minutes of the nominal time of satellite overpass (12:00 hrs for OCM-2). For a given location, an average of 10 samples was taken for each measurement grid points and the instrument was run in the reflectance mode by measuring target reflectance with respect to a perfectly white, diffuse, calibrated Spectralon panel.

Table 1: Instruments used for the calibration campaign

Sr. No.	Instrument	Parameter measured
1	Analytical Spectral Device	Hyper-spectral surface reflectance
2	MicroTOPS-II	Columnar aerosol optical depth, water vapour, and ozone
Low reflectance ocean site		
3	Satlantic Radiometer	Hyper-spectral radiance, irradiance of surface and sub-surface
4	Three channel fluorometer	Chlorophyll-a concentration, coloured dissolved organic matter

The field measured hyper-spectral reflectance as function of wavelength over the site is shown in Figure 1. The mean surface reflectance and one standard deviation are displayed over the full range of surface reflectance (350 – 2500nm), while Figure 2 displays for the OCM2 band width. Earlier

studies by Sridhar et. al., 2013 and Piyush et al., showed that this site has consistent temporal spectral signature. As shown in Figure 1, the site has a high reflectance greater than 0.3 for wavelength greater than 700nm and spectrally flat from 800nm to 2200nm. It also is highly spatially uniform, with less than 5% variation from 500 to 2500nm.

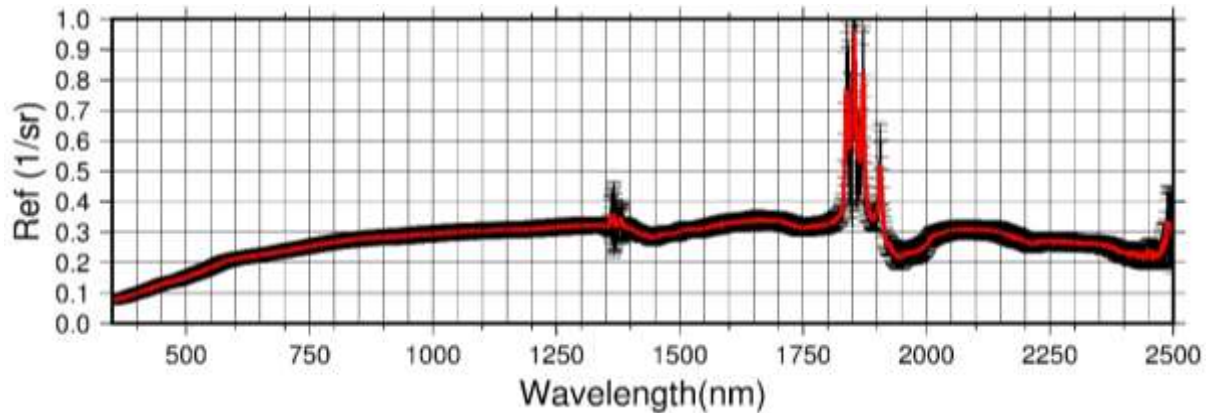


Figure 1: Surface reflectance as measured using ASD hyper-spectral radiometer over the 5x5 grid box over Little Rann of Kuchchh.

The atmosphere over the experimental site is that of a typical semi-arid, desert atmosphere in case of Little Rann of Kuchchh site. Measurements of aerosol optical depth (AOD), columnar water vapor and ozone contents were carried out at the above sites within ± 1 hour of satellite pass over the study area, using a Microtops-II sun-photometer. For a location, the sun-photometer computes AOD at six wavelengths, viz., 380, 440, 500, 675, 870 and 1020nm from measurements of atmospheric attenuation of direct beam of the sun. For each measurement, three rapid readings spaced at few seconds are taken and the mean of lowest AOD for a particular location and time is computed. The ozonometer measures total ozone content of the atmosphere based on ozone absorption at 3 wavelengths, 305, 312 and 320nm in the UV bands and total columnar water vapor is computed on basis of measurements at 936nm (peak absorption) and 1020nm (no absorption).

The measured values of AOT, water vapor and ozone for the study site during the study period and at over pass time of OCM2 sensors is given in Table 2.

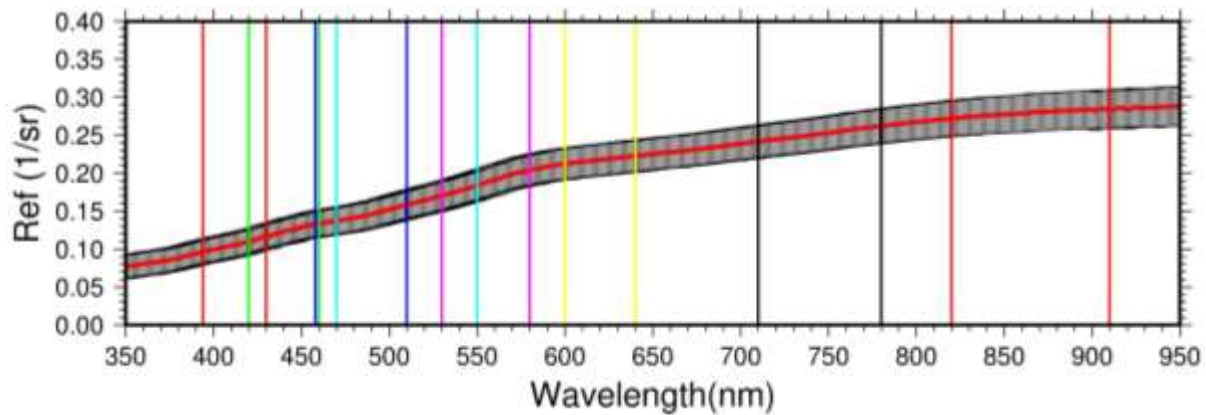


Figure 2: Surface reflectance as measured using ASD hyper-spectral radiometer for all OCM2 spectral bands over the 5x5 grid box over Little Rann of Kuchchh.

Figure 2b shows the derived water leaving radiance (L_w) using Satlantic hyper-spectral profiling radiometer on 27th February 2018 and on 1st March 2018. The solid curve depict the mean value and error bar shows the standard deviation among the multiple casts taken during these days. The spectral L_w shows peak values over blue region and trough over the green and red portion of the spectrum, which is the characteristics nature of the Case-1 waters (the water characteristics of water is controlled by the concentration of phytoplankton and its associates). These profiles are processed at 1nm interval using, ProSoft package, for further usage.

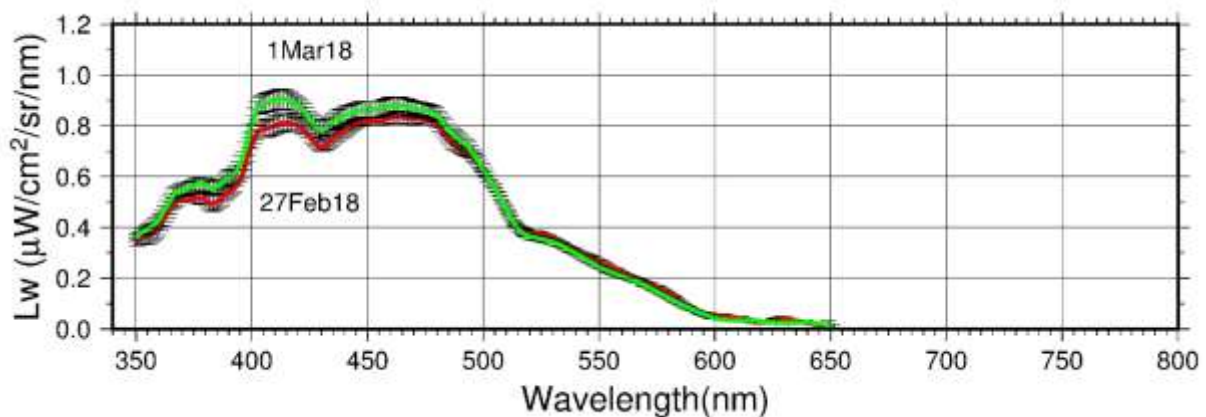


Figure 2a: Water leaving radiance derived from Satlantic radiometer measurements over Kavaratti Island on 27th February 2018 and 1st March 2018.

Table 2: AOD, WV and Ozone measurements from MicroTOPS-II during the overhead pass of OCM2 sensor.

Date	Time	AOD (870nm)	WV (cm)	O ₃ (DU)
------	------	-------------	---------	---------------------

04/01/2018	12:00	0.133	0.72	258.0
27/02/2018	12:00	0.202	1.62	193.4
01/03/2018	12:00	0.203	1.68	194.2
25/03/2018	12:00	0.156	0.79	360.8
27/03/2018	12:15	0.194	0.95	345.4



Figure 3: Actual field condition of Little Rann of Kuchchh (the high reflectance target)



Figure 4: Actual field condition of Kavaratti (the low reflectance target)

The Satlantic under water hyper-spectral radiometer is used in profiling mode to estimate the upwelling radiance and down welling irradiance component of sun light inside the ocean. The Figure 4 shows the radiometer in deployed condition at Kavaratti. Water leaving radiance (L_w)

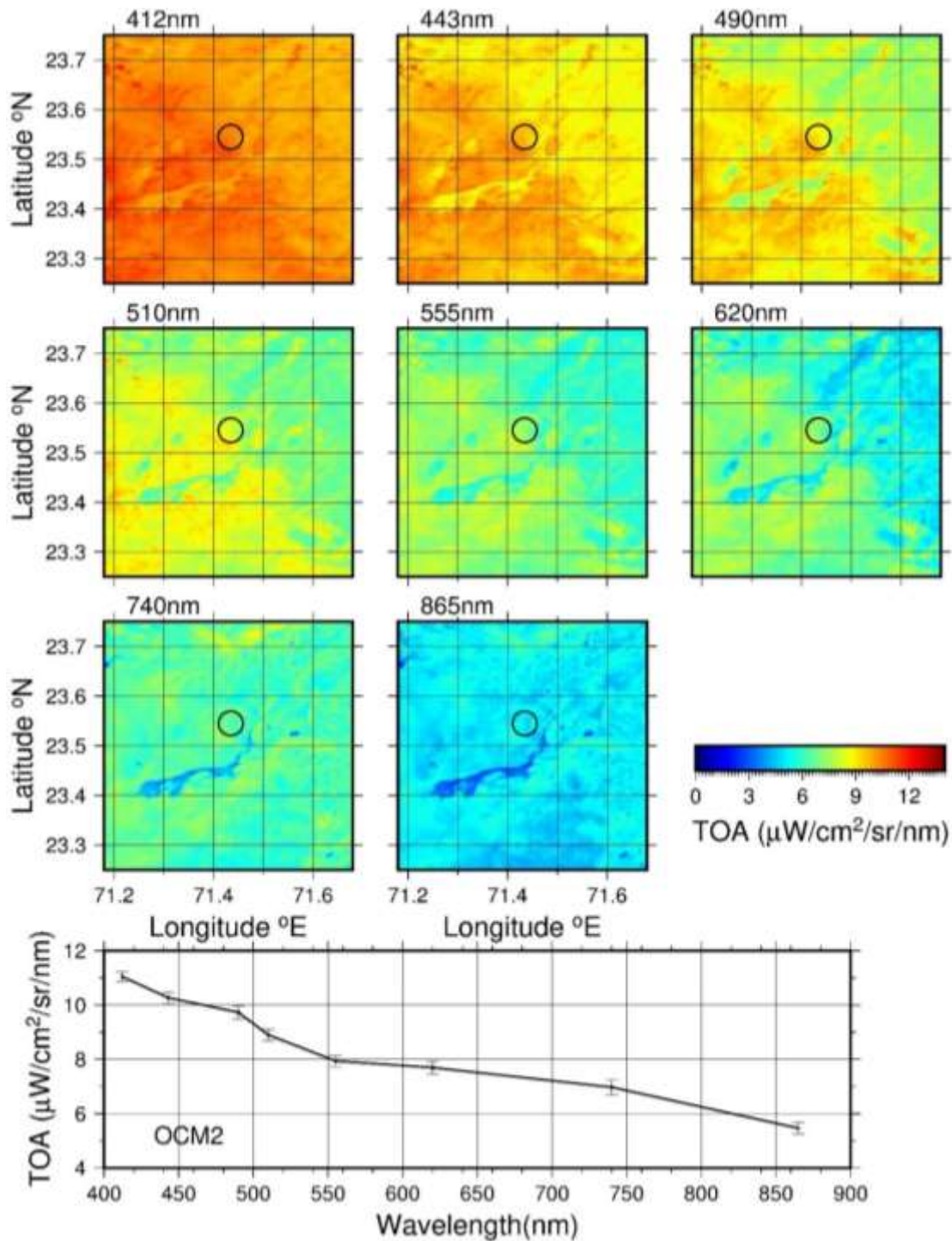


Figure 5a: OCM 2 top-of-the-atmosphere radiance as observed on 4th January 2018 over Little Rann of Kuchchh.

describes apparent optical property of the water and it is the signal that contains information about sea water constituents which is measured by ocean colour monitor type of sensors from space.

Therefore, most of the empirical approaches for retrieval of oceanic constituents from space sensor require this component of sun light.

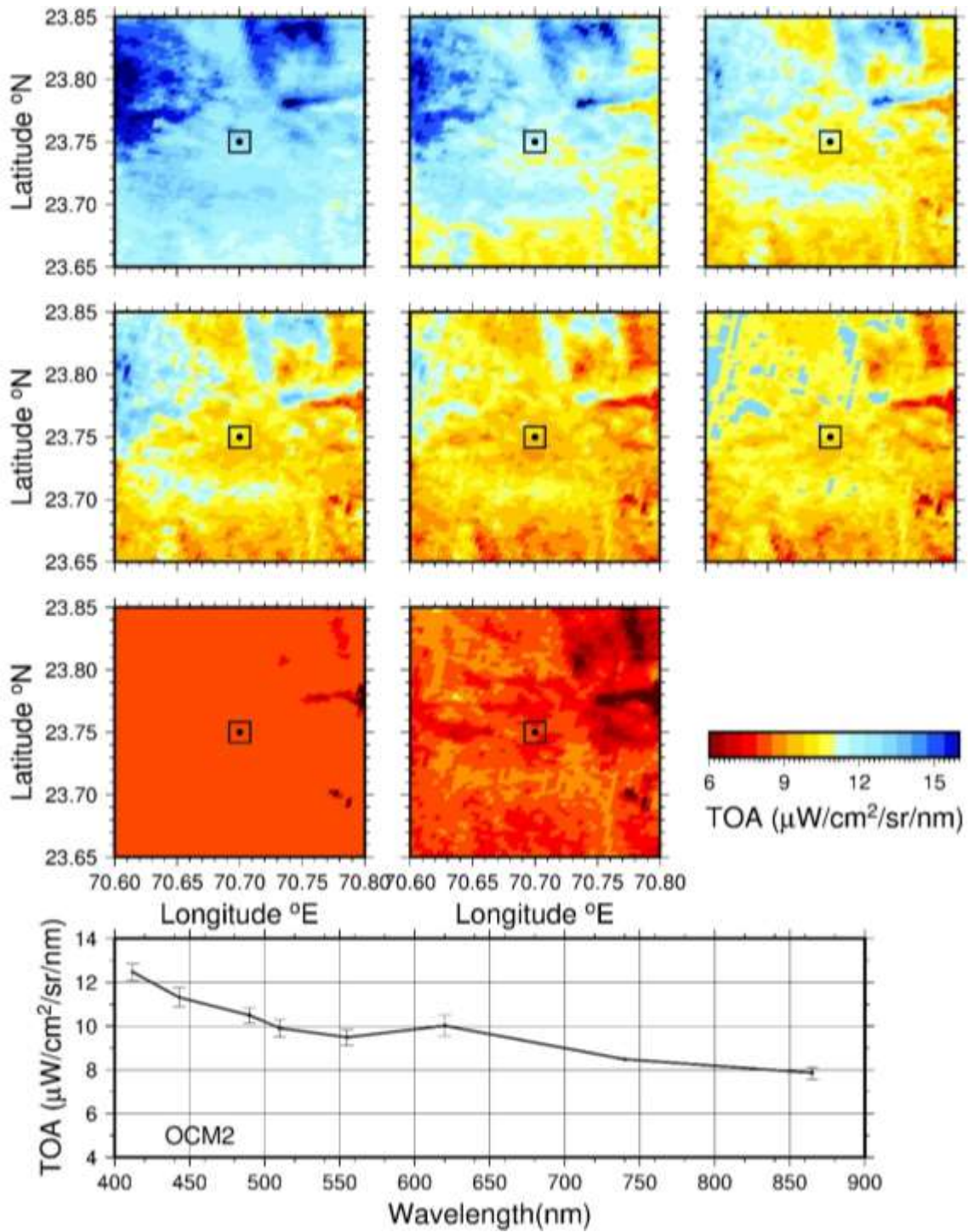


Figure 5b: OCM 2 top-of-the-atmosphere radiance as observed on 25th March 2018 over Greater Rann of Kuchchh (Desalpar).

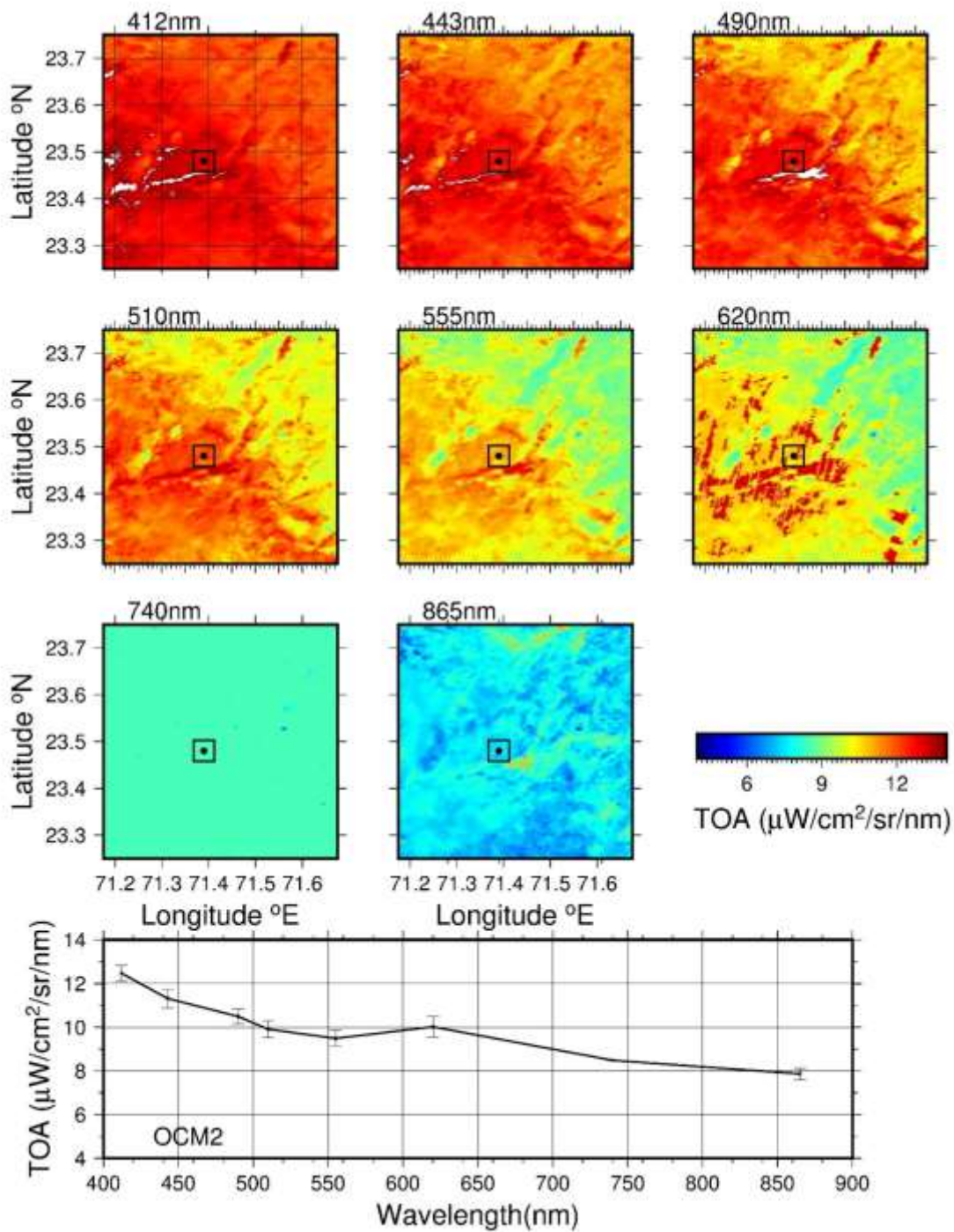


Figure 5c: OCM 2 top-of-the-atmosphere radiance as observed on 27th March 2018 over Little Rann of Kuchchh.

Typical OCM2 L1B radiance images of the experimental site along with acquisition dates are shown in Figure 5a, 5b, 5c in case of ocean site Figure 6a, 6b. The study sites are marked with black circle and field measurements are carried out within these geo-locations. The OCM2 L1B

products from NRSA, Hyderabad are used for deriving vicarious gain coefficients. We excluded data which are having band 8 (865nm) radiance greater than $1\mu\text{W}/\text{cm}^2/\text{sr}/\text{nm}$ (in case of ocean

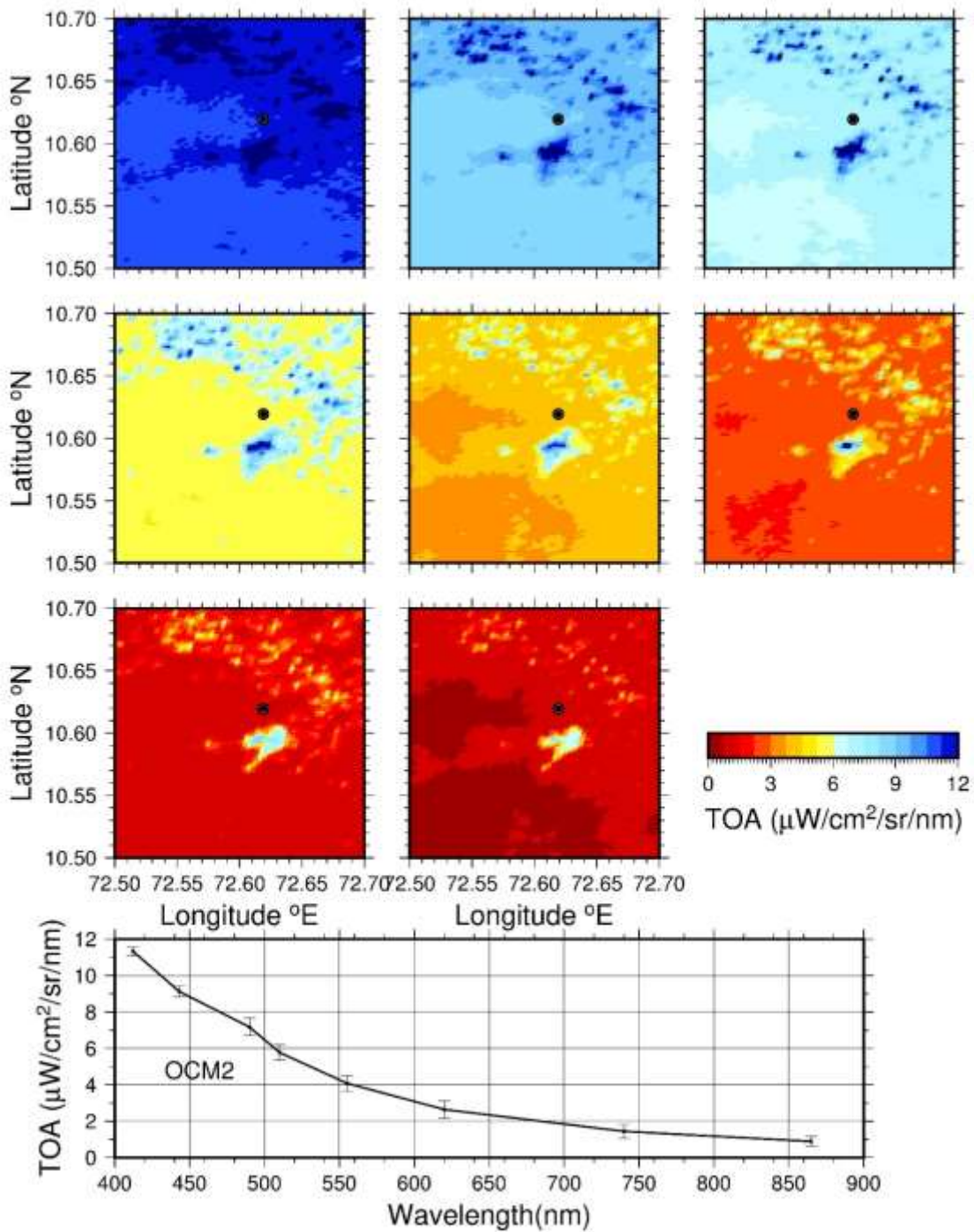


Figure 6a: OCM 2 top-of-the-atmosphere radiance as observed on 27th February 2018 over Kavaratti.

target), and measured aerosol optical thickness at this wavelength greater than 0.2. The sun and sensor geometry over Kavaratti, and other sites are taken from the header information of OCM2 L1B product.

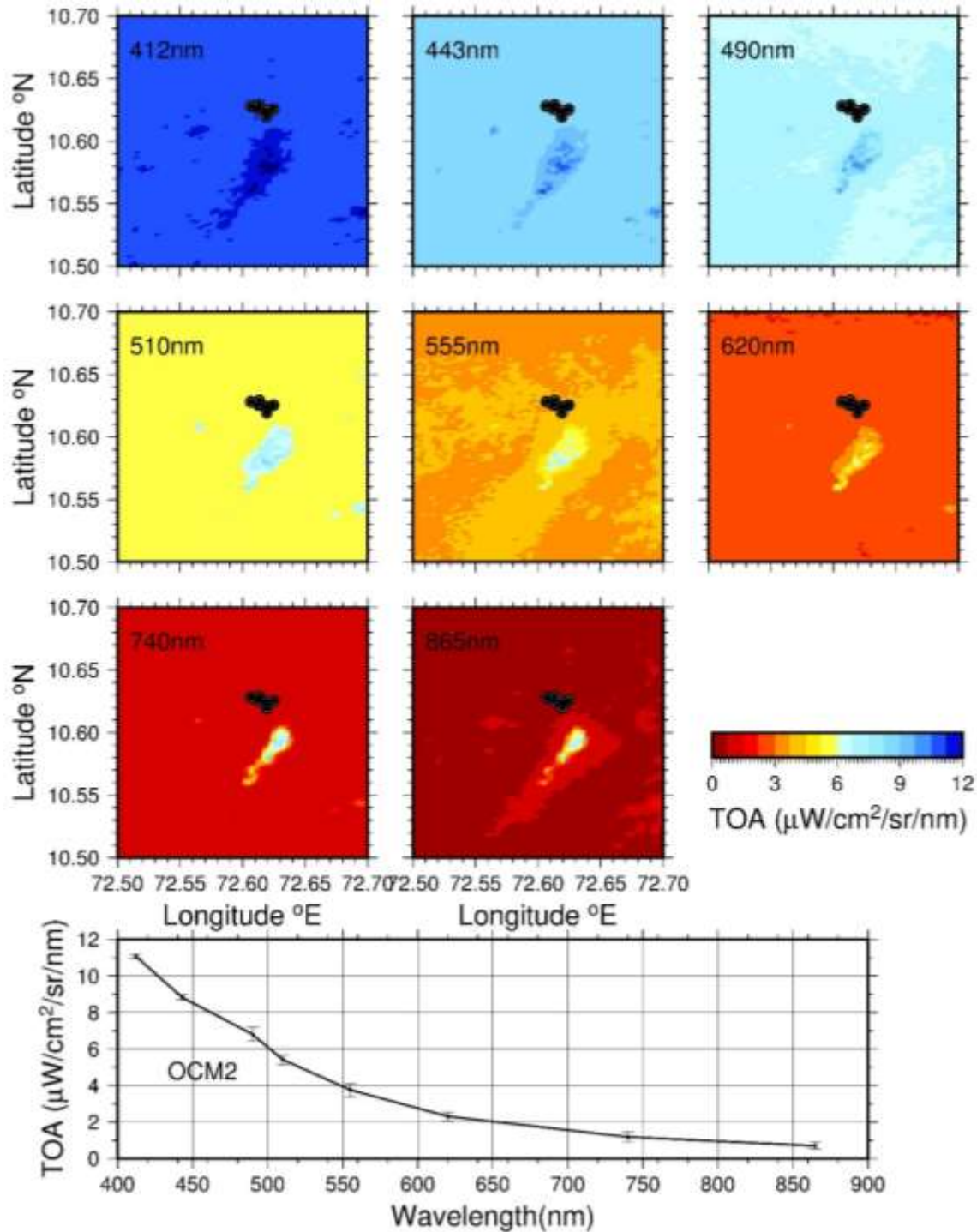


Figure 6b: OCM 2 top-of-the-atmosphere radiance as observed on 1st March 2018 over Kavaratti.

4. Satellite data used

The satellite data of OCM2 sensor on-board OceanSat-2 is used in this analysis. OCM2 is an 8-band multi-spectral camera operating in the visible-near-infrared spectral range with each band having an independent lens assembly for imaging onto the CCD camera in the focal plane. Hence, the eight bands were imaged independently. The full bandwidth was used to compute TOA radiances in this study, as the spectral response function is not exactly Gaussian in shape (Figure 7) and hence the concept of full width at half maximum may not be accurate for defining an

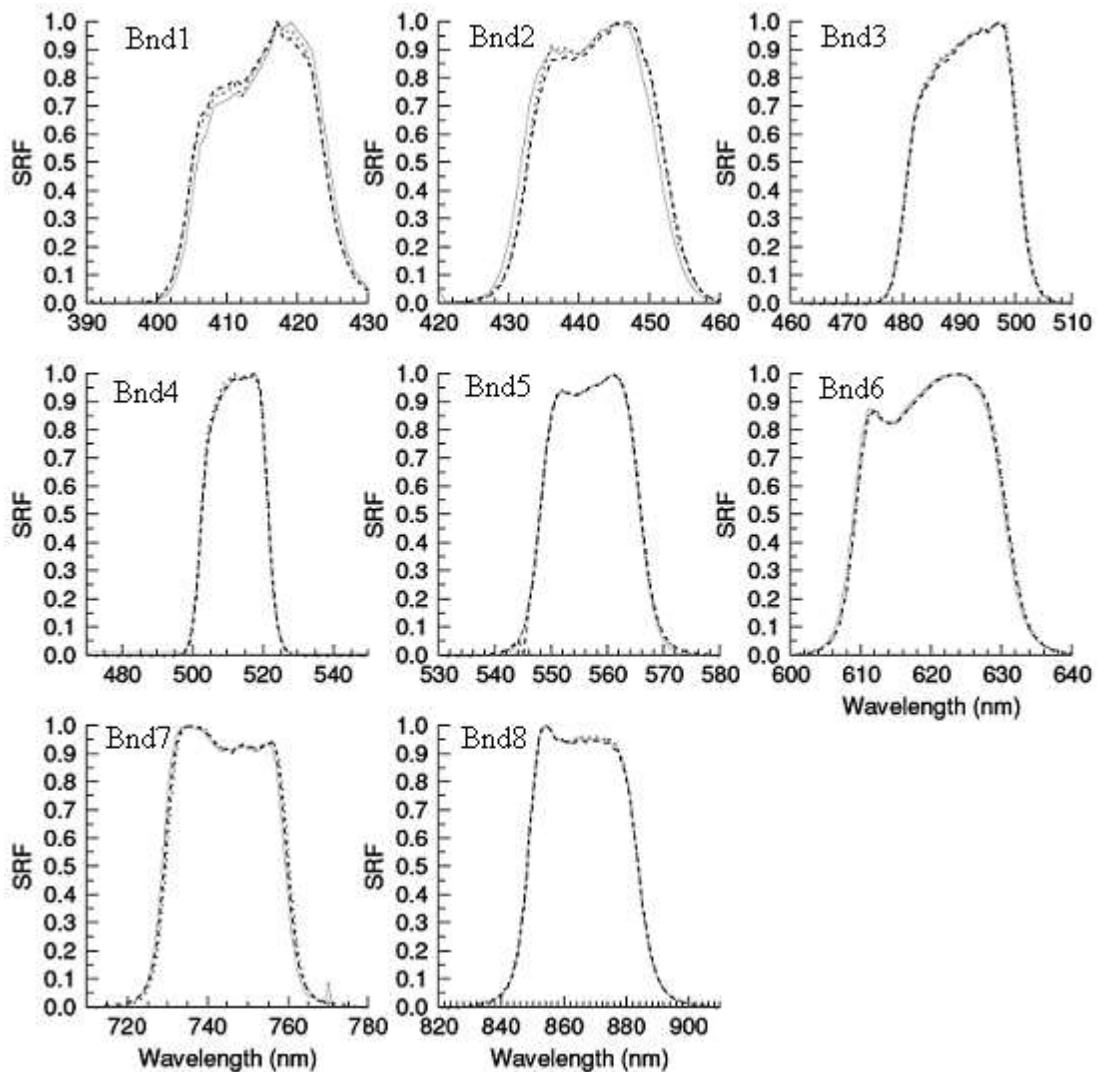


Figure 7: SRF of 8 bands of OCM-2 plotted as function of wavelength.

effective bandwidth. OCM2 provides an instantaneous geometric field of view of 360m and ground sampling distance of 236m (along track) covering a swath width of 1420km. Each lens

assembly contains a linear array charge coupled device (CCD) of 6000 pixels in the focal plane and the spectral band-pass filter in front of the CCD. Out of 6000 pixels, 3730 pixels in the centre are used to cover the image field. To avoid sun glint due to specular reflection from the ocean surface, there is provision to tilt the OCM2 by $\pm 20^\circ$ in the along-track direction. On-board calibration scheme using light-emitting diodes mounted near each CCD is incorporated to study long-term stability of the radiometric performance (Venkata Rao, 2010). The major specifications of OCM2 is given in Table 3.

Table 3: Major specifications of Ocean Colour Monitor-2

Parameter	Specifications
GIFOV (km)	0.360 x 0.236
Swath (km)	1420
Repetivity (days)	2
Local time of pass	12 noon \pm 10 min
Altitude (km)	720
Along-track steering	$\pm 20^\circ$
Spectral bands (nm)	402-422 433-453 480-500 500-520 545-565 610-630 725-755 845-880
Quantization	12 bits

For each in-situ record, corresponding local area coverage resolution satellite data file is identified and a nominal $2^\circ \times 2^\circ$ box centered over the in-situ location is extracted from the full satellite file. The Figures 5 and 6 show such plots of OCM2 radiance over the site and the bottom panel of line plot shows the radiance exactly over the measurement location. The satellite data were navigated to identify the pixel that corresponds with each in-situ location. Here, the in-situ data were collocated exactly when the satellite views the site. Restricting the box of odd dimensions to maintain the location of interest in the center of the box suggests a size of 7×7 image pixels. A statistical analysis on homogeneity test indicates that the use of 7×7 pixels box does not significantly degrade the result. We desire a small sampling box as we assume that as box size increases, geophysical variability may be introduced and thus violating the requirement of homogeneity of the site. We ultimately selected a 5×5 pixels box to limit the inaccuracy posed by

geophysical variability and errors in navigation while maintaining a reasonably small sampling area.

5. Screening of data set for vicarious calibration

The remainder of the exclusion criteria applied is based on the Level 2 processing flags set by the atmospheric correction algorithm (Franz, 2005). The exclusion criteria applied is shown in **Figure 8**. The flags are used to identify and exclude questionable pixels from the 5x5 box. Pixels are masked if any one of the following is met: land, cloud or ice, stray light, sun glint, high top-of-atmosphere radiance (865nm TOA radiance greater than $1\mu\text{W}/\text{cm}^2/\text{sr}/\text{nm}$). In addition, match ups for which a high variability (coefficient of variance is greater than 10%) around the site is detected and discarded too. For each match up, the in-situ value is computed as the average measures taken over a 2hr time slot ($\pm 1\text{hr}$ from the satellite overpass). A minimum of 50% of the pixels in the defined box are to be valid (i.e. unflagged) to ensure statistical confidence in the mean values retrieved. The presence of thin cloud is rejected based on observed aerosol optical thickness at 870nm (greater than 0.20).

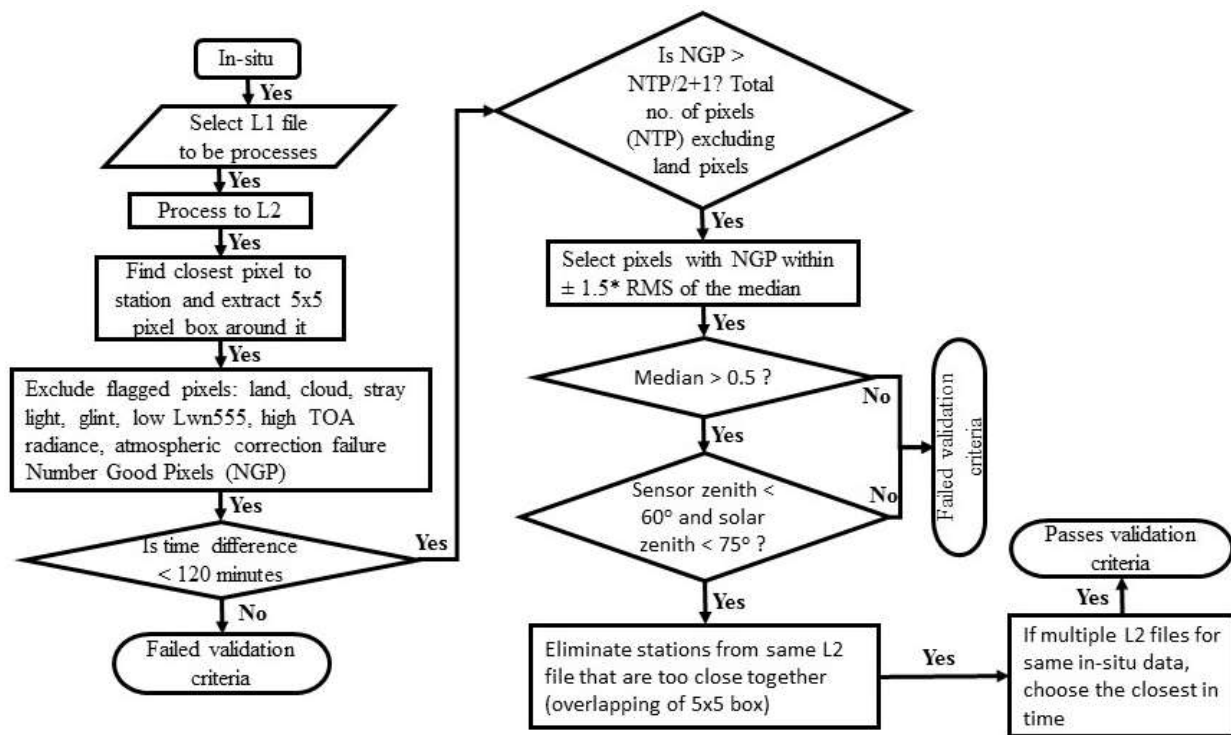


Figure 8: Flowchart of the matchup process highlighting the applied exclusion criteria.

To minimize the effect of outliers on the calculated mean value, especially for the case of coastal locations where the required minimum pixel count is reduced, a filter mean value is also calculated:

$$\text{Filter mean} = \frac{\sum_i (1.5 * \sigma - \bar{X}) < X_i < (1.5 * \sigma + \bar{X})}{N}$$

Where \bar{X} is the unfiltered mean value, σ is the standard deviation of the unfiltered data and N is the number of values within $\pm 1.5 * \sigma$.

6. Methodology: vicarious calibration

6.1 High reflectance land target

Reflectance-based and radiance-based techniques are the most common approaches while in-situ data sets are used for calibrating satellite sensors (Slater et. al., 1987). Reflectance-based technique is used in this study in case of the high reflectance land target, because it is difficult to maintain the radiometric accuracy of the spectrometer that measures the surface radiance in the radiance-based technique. The reflectance-based technique mainly depends on the measured ground surface reflectance. The reflectance is characterized by the ratio of measurement of the site to those of a standard reflectance/ Spectralon panel for which the bidirectional reflectance factor is precisely determined. The vicarious radiometric calibration depends on the surface reflectance and radiance from the sun to earth's surface and earth's surface to sensor and atmospheric optical thickness over the calibration site at the time of satellite pass.

The ground measurements are used as an input for radiative transfer (RT) code for the simulation of absolute radiances in the required bands (as listed in Table 3) at the sensor level. Apart from field measurements, additionally 6SV2.1 (here after 6S) code requires the geometric conditions, including the viewing zenith, viewing azimuth, solar zenith and solar azimuth angles. Viewing zenith and viewing azimuth angles are obtained from satellite metadata files and solar zenith and solar azimuth angles are calculated using time and location for a given data point. Figure 9 describes the flow chart of TOA spectral radiance simulation and estimation of calibration coefficient. We considered the continental aerosol model as a better representation of aerosol over calibration sites, which is the basic model over the land site.

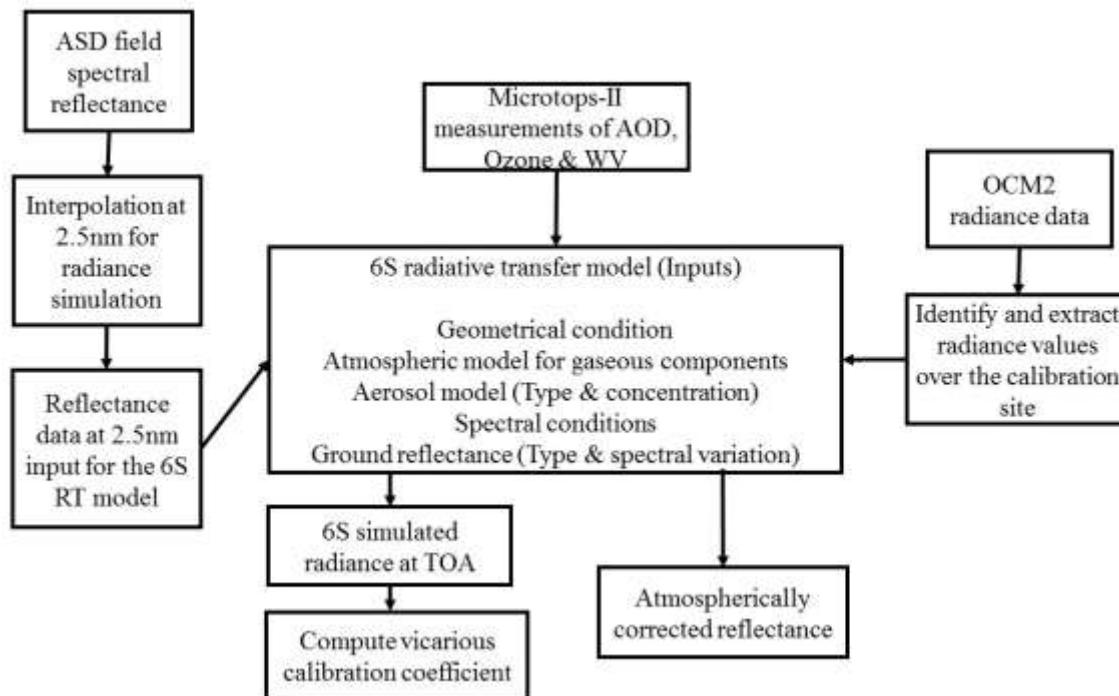


Figure 9: Detailed flow chart for the estimation of TOA radiance.

In the 6S code, when measured values of water vapor and ozone are given as input, the code assumes the US62 standard atmosphere profile for computations. The US62 atmosphere profile gives pressure, temperature, water vapor and ozone concentrations as function of height (up to 100 km), at discrete intervals of 34 layers. The continental aerosol model consists of mixture of dust-like, water soluble and soot components in fixed proportions. For a given aerosol model, the code computes the extinction coefficient, single scattering albedo, asymmetry parameter and the phase function using Mie theory. In the forward mode, the 6S code computes TOA reflectance and radiance for given surface reflectance, while in the inverse mode; the code computes the atmosphere corrected surface reflectance, for the same atmospheric parameters as in the forward model, for a given TOA at-satellite radiance input. The 6S code is a point based code (and not an image based code), i.e., the inputs are given for a single pixel. As mentioned in earlier, 25 field spectral measurements were done at the experimental site within approximately ± 1 hr of satellite pass. 6S TOA simulation was performed at individual points of reflectance measurement and mean, standard deviation of OCM-2 TOA radiance, 6S model TOA radiance is calculated. It is

assumed here that the 6S simulated radiance is the 'true' value. The vicarious calibration gain is defined as 6S/OCM2.

The comparison of spectral TOA radiance measured by OCM2 sensor and the 6S simulation is shown in Figure 10.

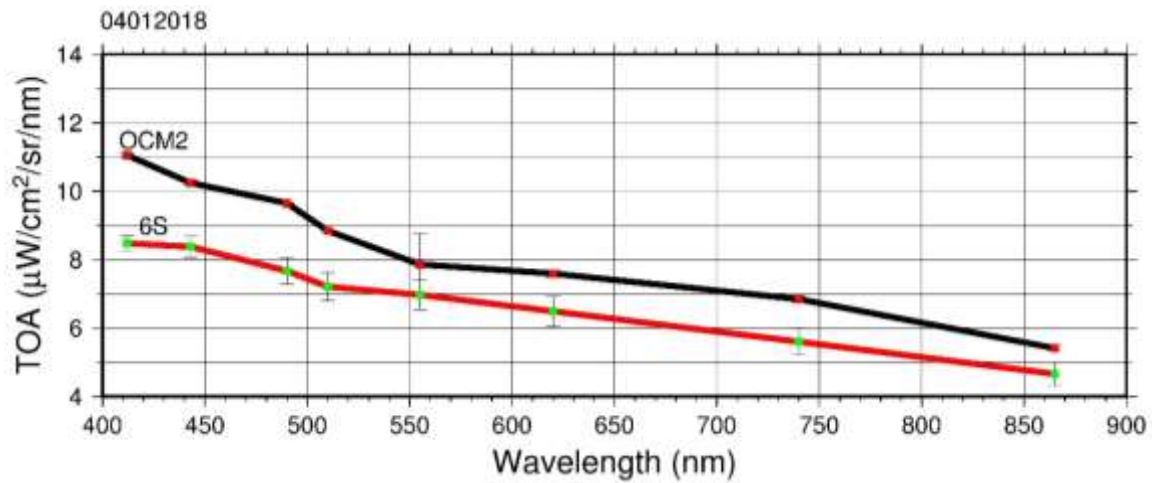


Figure 10a: OCM2 and 6S simulation over Rann of Kuchchh.

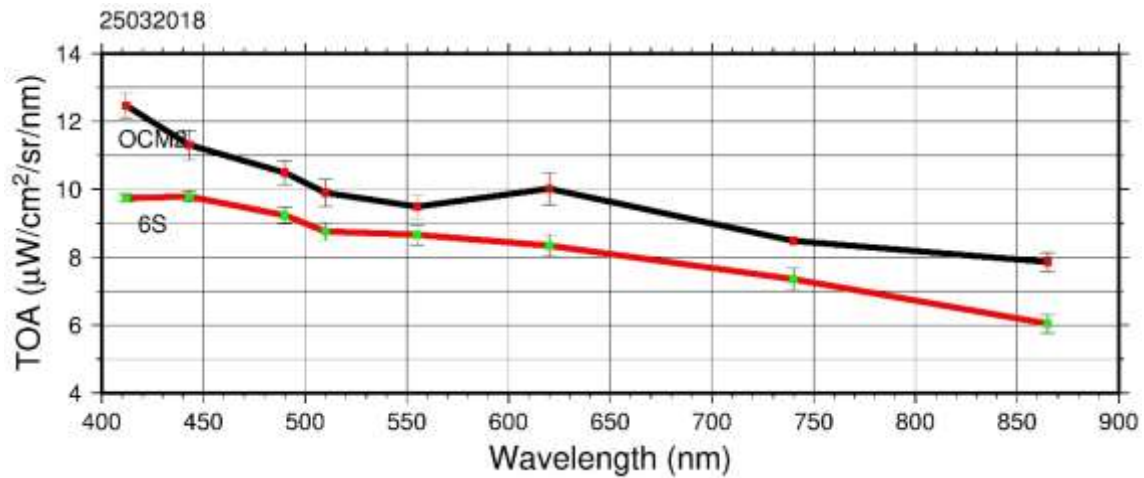


Figure 10b: Continuation ...

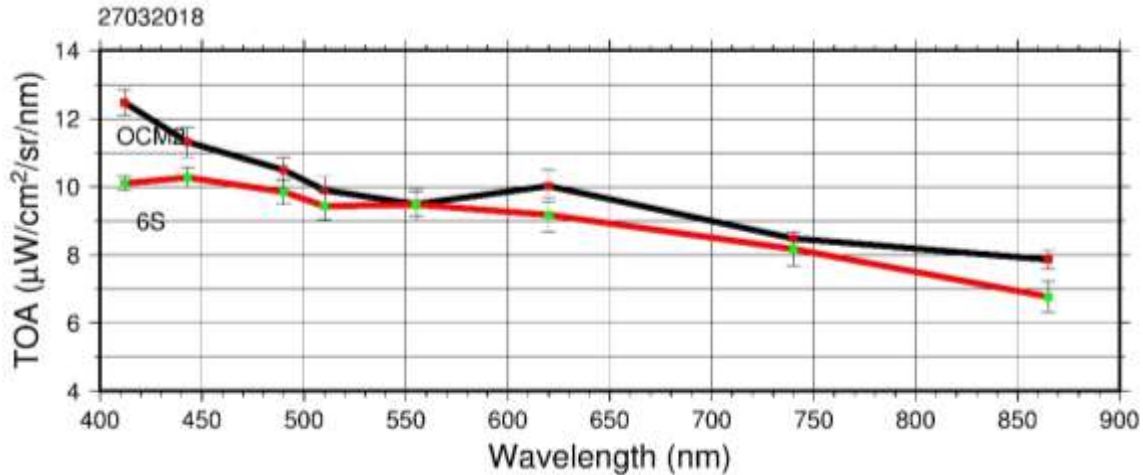


Figure 10c: Continuation ...

Table 4a: OCM2 and 6S TOA in 5x5 pixel box over Amarapur cal-val site (04/01/2018).

Band (nm)	OCM-2 (TOA) mean/stdev (Wm ⁻² sr ⁻¹ μm ⁻¹)	6S (TOA) mean/stdev (Wm ⁻² sr ⁻¹ μm ⁻¹) 25 model run	Gain coeff. (6S/OCM-2)
412	11.051/0.068	8.474/0.234	0.767
443	10.242/0.076	8.373/0.302	0.818
490	9.649/0.096	7.667/0.388	0.795
510	8.841/0.09	7.202/0.402	0.815
555	7.856/0.9	6.966/0.436	0.887
620	7.588/0.10	6.482/0.428	0.854
740	6.841/0.096	5.595/0.394	0.818
865	5.405/0.078	4.652/0.351	0.861

Table 4b: OCM2 and 6S TOA in 5x5 pixel box over Desalpar cal-val site (25/03/2018)

Band (nm)	OCM-2 (TOA) mean/stdev (Wm ⁻² sr ⁻¹ μm ⁻¹)	6S (TOA) mean/stdev (Wm ⁻² sr ⁻¹ μm ⁻¹) 265 model run	Gain coeff. (6S/OCM-2)
412	12.63/0.41	9.74/0.12	0.77
443	11.47/0.46	9.79/0.17	0.85
490	10.64/0.39	9.23/0.24	0.87
510	10.08/0.44	8.76/0.25	0.87
555	9.72/0.41	8.66/0.29	0.89
620	10.19/0.65	8.34/0.32	0.82
740	8.48/0.01	7.35/0.31	0.87
865	7.92/0.29	6.04/0.27	0.76

Table 4c: OCM2 and 6S TOA in 5x5 pixel box over Amarpur cal-val site (27/03/2018)

Band (nm)	OCM-2 (TOA) mean/stddev (Wm ⁻² sr ⁻¹ μm ⁻¹)	6S (TOA) mean/stddev (Wm ⁻² sr ⁻¹ μm ⁻¹) 25 model run	Gain coeff. (6S/OCM-2)
412	12.00/0.16	10.10/0.20	0.84
443	11.26/0.23	10.27/0.28	0.91
490	10.59/0.33	9.85/0.38	0.93
510	9.98/0.35	9.43/0.41	0.94
555	8.94/0.38	9.47/0.48	1.06
620	8.67/0.47	9.17/0.51	1.06
740	8.48/0.06	8.17/0.49	0.96
865	7.14/0.46	6.77/0.45	0.95

6.2 Vicarious calibration (low reflectance ocean target)

The model adopted for computing TOA radiance was derived from the equation governing the basic ocean color sensor measurement, the radiative transfer equation for the radiance observed in orbit. In practice, the vicarious calibration equates the top-of-the-atmosphere radiance over the ocean with the radiances as measured by ocean color sensor. The top-of-the-atmosphere radiance over the ocean is given by (Gordon, 1998):

$$L_t(\lambda) = L_r(\lambda) + L_a(\lambda) + L_{ra}(\lambda) + T(\lambda)L_g(\lambda) + t(\lambda)L_{wc}(\lambda) + t(\lambda)L_w(\lambda) \quad (9)$$

where, λ is the wavelength of the measurement, L_r is the Rayleigh radiance resulting from multiple scattering by air molecules in the absence of aerosols, L_a is the radiance arising from multiple scattering by aerosols in the absence of air, L_{ra} is the radiance arising from the interaction of molecular and aerosol scattering, L_g is the glint radiance arising from the specular reflection of the sun on the water surface, L_{wc} is the whitecap radiance, L_w is the water-leaving radiance, T is the direct transmittance of the atmosphere, and t is the diffuse transmittance of the atmosphere. The term L_{ra} accounts for the interaction between Rayleigh and aerosol scattering, e.g., photons first scattered by air then scattered by aerosol, or photons first scattered by aerosols then by the air. This term is zero in the single-scattering case, in which photons are only scattered, and can be ignored as long as the amount of multiple scattering is small, i.e., at small Rayleigh and aerosol optical thicknesses.

In principle the radiances $L_{as}(\lambda) = L_a + L_{ra}$ could be removed if optical properties of the aerosol are known. Over the open ocean the atmosphere can be very clear with most of the aerosol generated

by local processes such as breaking waves. Under such conditions, a simple atmospheric correction algorithm that employs a multiple-scattered Rayleigh component and a singly-scattered aerosol component can be used (Gordon, 1997; Gordon, and Clark, 1981; Gordon, and Castano, 1987). Equation-9 thus becomes:

$$L_t(\lambda) = L_r(\lambda) + L_{as}(\lambda) + t(\lambda)L_w(\lambda) + T(\lambda)L_g(\lambda) + t(\lambda)L_{wc}(\lambda) \quad \text{---- (10)}$$

Hence, the uncertainty in the top-of-the-atmosphere radiance is as a result of the uncertainties in singly-scattered aerosol component, water-leaving radiance (due to sea-water constitutions) and whitecap radiance.

For non-sun glint days equation (2) can be written as:

$$L_t(\lambda) = L_{path}(\lambda) + (\lambda)L_{wc}(\lambda) + t(\lambda)L_w(\lambda), \quad \text{---- (11)}$$

Using single scattering approximation, L_r is given by:

$$L_r = \tau_r(\lambda)F'_0(\lambda)P_r(\theta, \theta_0, \lambda)/4\pi, \quad \text{---- (12)}$$

Where

$$P_r(\theta, \theta_0, \lambda) = \{P_r(\theta_-, \lambda) + [\rho(\theta) + \rho(\theta_0)]P_r(\theta_+, \lambda)\}/\cos\theta, \quad \text{---- (13)}$$

$$\cos\theta_{\pm} = \pm\cos\theta_0\cos\theta - \sin\theta_0\sin\theta\cos(\varphi - \varphi_0), \quad \text{---- (14)}$$

θ_0 and φ_0 are, respectively, the zenith and azimuth angles of a vector from the point on the sea surface under examination (pixel) to the sun, θ and φ are the zenith and azimuth angles of a vector from the pixel to the sensor. $\rho(\theta)$ is the Fresnel reflectance of the interface for an incident angle θ , $P_r(\alpha, \lambda)$ is the Rayleigh scattering phase function,

$$P_r(\alpha) = \frac{3}{4}[1 + \cos^2\alpha], \quad \text{---- (15)}$$

and $\tau_r(\lambda)$ is Rayleigh optical thickness. $F'_0(\lambda)$ is the instantaneous extraterrestrial solar irradiance $F_0(\lambda)$ reduced by two trips through the ozone layer, i.e.,

$$F'_0 = F_0 \exp\left[-\tau_{oz}\left(\frac{1}{\cos\theta} + \frac{1}{\cos\theta_0}\right)\right]d^2, \quad \text{---- (16)}$$

where, τ_{oz} is the ozone optical thickness and d is the variation in sun-earth distance. Hansen and Travis (1974) derive optical thickness, τ_{r0} , at the standard atmospheric pressure P_0 of 1013.25 mbar as:

$$\tau_{r0} = 0.008569\lambda^{-4}(1 + 0.0113\lambda^{-2} + 0.00013\lambda^{-4}), \quad \text{---- (17)}$$

λ is the wavelength in μm . At any other surface pressure, Rayleigh optical thickness is:

$$\tau_r = \frac{P}{P_0} \tau_{r0} \quad \text{---- (18)}$$

The diffuse transmittance t of the atmosphere is given approximately by (Gordon, et. al., 1983)

$$t = \exp\left[-(\tau_r / 2 + \tau_{oz}) / \cos\theta\right] \quad \text{---- (19)}$$

The radiance due to aerosol single scattering is expressed as:

$$L_{as} = \rho_{as} \left(\frac{F_0 \cos\theta_0}{\pi} \right) \quad \text{---- (20)}$$

where,

$$\rho_{as}(\lambda) = \omega_a(\lambda) \tau_a(\lambda) P_a(\theta, \theta_0, \lambda) / 4 \cos\theta \cos\theta_0,$$

$$P_a(\theta, \theta_0, \lambda) = P_a(\theta_-, \lambda) + [r(\theta) + r(\theta_0)] P_a(\theta_+, \lambda)$$

The parameters $\tau_a(\lambda)$, $\omega_a(\lambda)$, and $P_a(\alpha, \lambda)$ are, respectively, the aerosol optical thickness, the aerosol single-scattering albedo, and the aerosol scattering phase function. The marine aerosols are assumed for parameter determination (Doerffer, 1992).

The whitecaps are related to environmental parameters and it is obvious to relate with wind speed W , and stability of the atmosphere ΔT . Following Monahan and O’Muircheartaigh (1986), whitecaps fraction is given by:

$$f = 1.95 \times 10^{-5} W^{2.55} \exp(-0.0861 \Delta T) \quad \text{---- (21)}$$

where, $\Delta T = T_A - T_W$, with T_A and T_W representing the air and water temperatures, respectively with $\Delta T > 0$ implying a stable atmosphere.

The whitecap reflectance is computed by using Koepke, 1984 formalism and is given below:

$$\rho_{wc}(\lambda) = 0.22 * f * t(\theta_0, \lambda) \quad \text{---- (22)}$$

The vicarious calibration for OCM2 spectral bands is performed by comparing the radiance measured by satellite sensor in each spectral band with contemporaneous top-of-the-atmosphere radiance calculated using the *in-situ* measurements. The sensitivity of this methodology is reported in “SAC/RESA/MESG/OCEANSAT-II/CAL-VAL-1/07”.

The resulting $L_t(\lambda)$ is compared to the satellite measured $L_t(\lambda)$ and a gain coefficient, g_λ , is derived that would force agreement of the measured $L_t^m(\lambda)$ and the vicarious $L_t^v(\lambda)$:

$$g_\lambda = \frac{L_t^{vicarious}(\lambda)}{L_t^{measured}(\lambda)}, \quad \text{---- (23)}$$

The final g_λ is determined as

$$\left[\sum_{j=1}^N g_\lambda(j) \right] / N, \quad \text{---- (24)}$$

where the index j refers to the individual g_λ values and N is the number of vicarious calibration points.

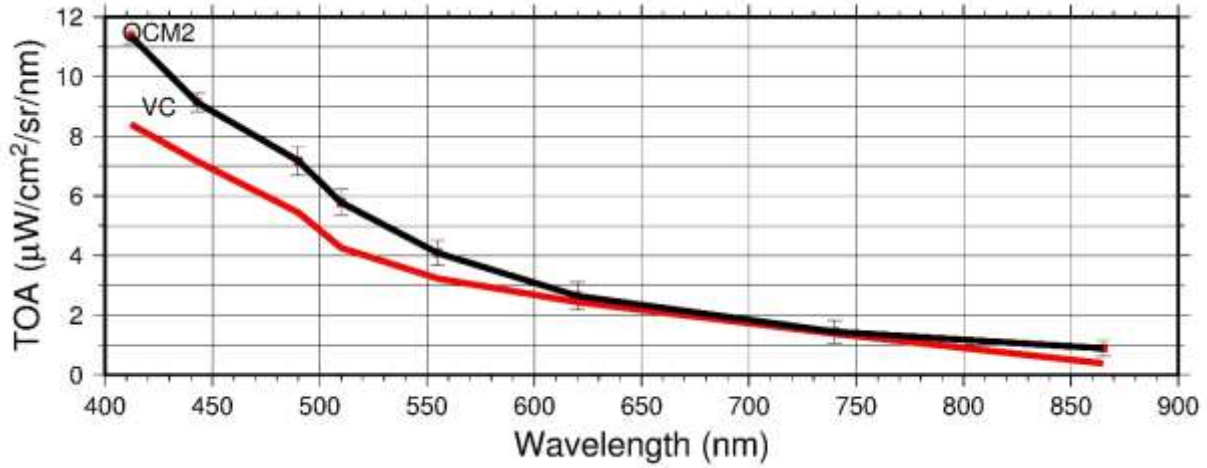


Figure 11a: The TOA radiance from OCM2 simulated using in-situ observations for 27th February 2018

Table 5a: OCM2 and 6S TOA in 5x5 pixel box over Kavaratti (27/02/2018)

Band (nm)	OCM-2 (TOA) mean/stdev (Wm ⁻² sr ⁻¹ μm ⁻¹)	VC (TOA) mean (Wm ⁻² sr ⁻¹ μm ⁻¹)	Gain coeff. (VC/OCM-2)
412	11.35	8.41	0.74
443	9.13	7.17	0.79
490	7.17	5.45	0.76
510	5.77	4.26	0.74
555	4.08	3.23	0.79
620	2.64	2.44	0.92
740	1.44	1.38	0.96
865	0.89	0.38	0.43

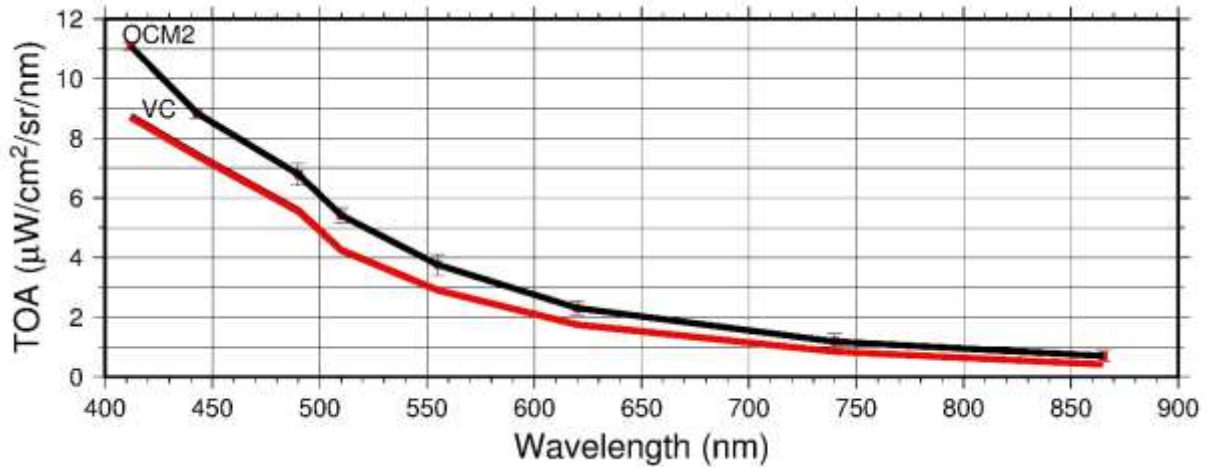


Figure 11b: The TOA radiance from OCM2 simulated using in-situ observations for 1st March 2018

Table 5b: OCM2 and 6S TOA in 5x5 pixel box over Kavaratti (01/03/2018)

Band (nm)	OCM-2 (TOA) mean (Wm ⁻² sr ⁻¹ μm ⁻¹)	VC (TOA) mean (Wm ⁻² sr ⁻¹ μm ⁻¹)	Gain coeff. (VC/OCM-2)
412	11.08	8.72	0.79
443	8.83	7.42	0.84
490	6.79	5.56	0.82
510	5.41	4.24	0.78
555	3.75	2.90	0.77
620	2.30	1.74	0.76
740	1.18	0.84	0.71
865	0.69	0.41	0.59

This report gives insight of OCM2 sensor performance over land site and ocean site for the year 2018 apart from ocean site calibration during the previous years. The analysis is done with two different radiative transfer simulation for the land and ocean sites which are explained earlier in this report and hence averaging the vicarious gain coefficients for the near infrared channels of OCM2 (band 7 & 8) may lead to large errors in geo-physical products. Since the emanating target energy beyond 650nm is nearly zero, the simulation of TOA radiance of OCM2 over Kavaratti water may lead to higher noise which are arising from the atmosphere above the target. In order to avoid such simulation results into the vicarious calibration gain coefficient computation, we

suggest the simulation results performed over land target may be considered for the bands 7 & 8 of OCM2 sensor. Accordingly, the average gain is shown in table 6.

Table 6: The mean vicarious calibration gain coefficient for OCM2

Band1	Band2	Band3	Band4	Band5	Band6	Band7	Band8
0.78	0.84	0.84	0.83	0.88	0.88	0.88	0.86

7. Conclusion

OCM2 is over estimating the TOA radiances over the land site. The land site TOA radiances are simulated with 6S vector radiative transfer model, which includes the polarization effect arising from Rayleigh and Mie particles. The ocean site TOA radiance are simulated through the radiative transfer calculation as described in this report, in this calculation the radiation due to polarization effect is not considered. Since the radiative component in TOA is much smaller in case of TOA simulation over low reflectance target like ocean, the bands 7 and 8 of OCM2 TOA radiances over ocean is avoided in calculating the vicarious gain coefficient. Table 6 shows the mean vicarious gain coefficient computed for all the eight bands of OCM2.

8. Acknowledgements

The project team members are grateful to Shri Thapan Misra, Director, SAC, for showing keen interest and for providing motivation for this study. We are grateful to Dr. Raj Kumar, Deputy Director, EPSA for encouragement. Authors also thank the director DST, Kavaratti for the project support.

9. References

1. Pagnutti, M. 2006. *Initial Radiometric Calibration of the AWiFs Using Vicarious Calibration Techniques*. USDA FAS/PECAD Seminar, Fairfax, Virginia, USA.
2. Thome, K. J. 2001. "Absolute Radiometric Calibration of Landsat 7 ETM+ Using the Reflectance Based Method." *Remote Sensing of Environment* 78: 27–38.

3. Chander, G., B. L. Markham, and D. L. Helder. 2009. "Summary of Current Radiometric Calibration Coefficients for Landsat MSS, TM, ETM+ and EO-1 ALI Sensors." *Remote Sensing of Environment* 113: 893–203.
4. Bruegge, C. J., D. J. Diner, R. A. Kahn, N. Chrien, M. C. Helmlinger, B. J. Gaitley, and W. A. Abdou. 2007. "The MISR Radiometric Calibration Process." *Remote Sensing of Environment* 107: 2–11.
5. Slater, P.N., Biggar, S.F., Holm, R.A., Jackson, R.D., Mao, Y., Moran, M.S., Palmer, J.M., Yuan, B., 1987. Reflectance- and radiance-based methods for in-flight absolute calibration of multispectral sensors. *Remote Sens. Environ.* 22, 11–37.
6. Gellman, D.I., Biggar, S.F., Slater, P.N., Bruegge, C.J., 1991. Calibrated intercepts for solar radiometers used in remote sensor calibration. *Proc. SPIE* 1493, 19–24.
7. Kotchenova, S.Y., Vermote, E.F., Levy, R., Lyapustin, A., 2008. Radiative transfer codes for atmospheric correction and aerosol retrieval: intercomparison study. *Appl. Opt.* 47 (13), 2215–2226.
8. Vermote, E.D., Tanre, J.L., Deuze, M., Herman, J.J., Morcrette, Kotchenova, S.Y., 2006. Second Simulation of Satellite Signal in the Satellite Spectrum (6S). 6S User Guide Version 3. University of Maryland.
9. Markham, B.L., Halthore, R.N., Goetz, S.J., 1992. Surface reflectance retrieval from satellite and aircraft sensors: results of sensor and algorithm comparison during FIFE. *J. Geophys. Res.* 97. (D17718), 7857795.
10. Gordon, H. R., 1998, In-orbit calibration strategy for ocean color sensors, *Remote Sensing of Environment*, 63, pp. 265–278.
11. Gordon, H. R., 1997. Atmospheric correction of ocean color imagery in the Earth observing system era, *Journal of Geophysical Research.* 102, 17,081-17,106.
12. Gordon, H. R., and Clark, D. K., 1981, Clear water radiances for atmospheric correction of coastal zone color scanner imagery, *Applied optics*, 20, pp. 4175-4180.
13. Gordon, H. R., and Castano, D. J., 1987, The coastal zone color scanner atmospheric correction algorithm: multiple scattering effects, *Applied optics*, 26, pp. 2111-2122.
14. Hansen, J. E., and Travis, L. D., 1974. Light scattering in planetary atmosphere, *Space Science Review*, 16, 527.

15. Gordon, H. R, Brown, J. W., Brown, O. B., Evans, R. H., and Clark, D. K., 1983. Nimbus-7 CZCS: Reduction of its radiometric sensitivity with time, *Applied Optics*, 24, 3929-3931.
16. Doerffer, R., 1992. Imaging spectroscopy for detection of chlorophyll and suspended matter: Fundamentals and prospective application, (eds) F. Toselli and J. Bodechtel (Kluwer Academic Publishers Dordrecht/Boston/London) 215-257.
17. Koepke, P., 1984, Effective reflectance of oceanic whitecaps, *Applied optics*, 23, 1816-1824.
18. Absolute vicarious calibration of OCM2 and AWiFS sensors using a reflectance based method over land sites in the Rann of Kutch, Gujarat. V.N. Sridhar, Kaushal B. Mehta, R.P. Prajapati, K. N. Babu, N.M. Suthar, and A.K. Shukla. *International Journal of Remote Sensing*, 2013, Vol. 34, No. 16, 5690–5708, <http://dx.doi.org/10.1080/01431161.2013.792967>.
19. Venkata Rao, M., OceanSat-2 mission and applications, Dept. of Space, Government of India, Bangalore, 2010, NNRMS (B)-34, pp. 1–6.
20. Franz, B.A.2005. Msl 12 user's guide. URL [http://oceancolor.gsfc.nasa.gov/DOCS/MSL 12](http://oceancolor.gsfc.nasa.gov/DOCS/MSL12).